

Interface-driven unusual anomalous Hall effect in $\text{Mn}_x\text{Ga}/\text{Pt}$ bilayersK. K. Meng^{1,*}, L. J. Zhu,² Z. H. Jin,³ E. K. Liu,⁴ X. P. Zhao,⁵ I. A. Malik,⁶ Z. G. Fu,⁷
Y. Wu,¹ J. Miao,¹ X. G. Xu,¹ J. X. Zhang,⁶ J. H. Zhao,⁵ and Y. Jiang^{1,†}¹*Beijing Advanced Innovation Center for Materials Genome Engineering, School of Materials Science and Engineering, University of Science and Technology Beijing, Beijing, China*²*Cornell University, Ithaca, New York 14853, USA*³*Department of Applied Physics, Graduate School of Engineering, Tohoku University, 6-6-05, Aoba-yama, 980-8579 Sendai, Japan*⁴*Institute of Physics, Chinese Academy of Sciences, Beijing, China*⁵*State Key Laboratory of Superlattices and Microstructures, Institute of Semiconductors, Chinese Academy of Sciences, Beijing, China*⁶*Department of Physics, Beijing Normal University, Beijing, China*⁷*Institute of Applied Physics and Computational Mathematics, Beijing, China*

(Received 18 July 2019; revised manuscript received 25 October 2019; published 11 November 2019)

The effects of spin-orbit coupling and symmetry breaking at the interface between a ferromagnet and heavy metal are particularly important for spin-based information storage and computation. Recent discoveries suggest they can create novel chiral spin structures (e.g., skyrmions), which have often been identified through the appearance of the bump/dip features of Hall signals, the so-called topological Hall effect (THE). In this work, however, we present an unusual anomalous Hall effect (UAHE) in $\text{Mn}_x\text{Ga}/\text{Pt}$ bilayers and demonstrate that the features extremely similar to THE can be generated without involving any chiral spin structures. Low-temperature magnetic force microscopy has been used to explore the magnetic field-dependent behavior of spin structures, and the UAHE as a function of magnetic field does not peak near the maximal density of magnetic bubbles. Our results unambiguously evidence that the UAHE in $\text{Mn}_x\text{Ga}/\text{Pt}$ bilayers shows no correlation with chiral spin structures but is driven by the modified interfacial properties, indicating a wealth of underlying and interesting physics.

DOI: [10.1103/PhysRevB.100.184410](https://doi.org/10.1103/PhysRevB.100.184410)**I. INTRODUCTION**

Interface-driven magnetic effects and phenomena associated with spin-orbit coupling (SOC) and intrinsic symmetry breaking at interfaces hold significant potential for spin-dependent electronic functionalities [1]. Effects at interfaces can be classified as emergent in the sense that complex unanticipated phenomena emerge from apparently simple materials and interactions, providing challenges of predictability and design of functionality [2,3]. It has only recently been appreciated that interfaces, particularly those where SOC is strong, can fundamentally change the magnetic ground states in the ferromagnet (FM)/heavy metal (HM) heterostructures. Owing to the presence of strong SOC and inversion asymmetry, Dzyaloshinskii-Moriya interaction (DMI), an antisymmetric exchange interaction that favors a chiral arrangement of the magnetization, will be generated [2–4]. It is in the form of $\mathbf{D}_{12} \cdot (\mathbf{S}_1 \times \mathbf{S}_2)$, where the vector \mathbf{D}_{12} represents the DMI strength; \mathbf{S}_1 and \mathbf{S}_2 are the total spin of two nearby atoms [5,6]. When the DMI is sufficiently strong compared to other interactions, it could lead to topologically protected (chiral) spin structures, such as skyrmions or skyrmion lattices [7]. Skyrmions can be defined by the topological number N , which is a scale of the winding of the normalized local magnetization, m . In the two-dimensional limit, the topological

number is $N = \frac{1}{4\pi} \int \mathbf{m} \cdot (\partial_x \mathbf{m} \times \partial_y \mathbf{m}) dx dy$ [3,7]. This non-trivial topological property governs some of the most important properties of skyrmions including the topological Hall effect (THE) [8–10]. When a conduction electron passes through a skyrmion, the spin of the conduction electron will adiabatically follow the texture and acquire a real-space Berry phase, which deflects the conduction electrons perpendicular to the current direction and causes an additional contribution to the observed Hall signals termed as THE, characterized by the appearance of bumps or dips in the Hall measurements. The effective magnetic field can be described by $B_{\text{eff}} = \frac{\hbar c}{2e} \hat{z} \mathbf{m} \cdot (\partial_x \mathbf{m} \times \partial_y \mathbf{m})$, which is closely related to the definition of topological number [3]. However, the above real-space Berry phase picture is valid only if the exchange coupling between electrons and local magnetization is strong (adiabatic approximation), while it fails in the weak coupling regime (nonadiabatic approximation) since the electrons fail to adjust their spin to the local magnetization and the spin-flip processes are activated [11–13]. In such a regime, the electrons will experience an inhomogeneous emergent field as there are randomly distributed chiral spin structures, in contrast to electrons in bulk systems which experience a systematically varying uniform emergent magnetic field due to the ordered arrangement of chiral spin structures such as skyrmion crystals [14].

In this work, however, we report an unusual anomalous Hall effect (UAHE) that can generate the same transport features of the THE without involving any chiral spin structures. Low-temperature magnetic force microscopy (MFM)

*kkmeng@ustb.edu.cn

†yjiang@ustb.edu.cn

results indicate that the additional Hall signals as a function of magnetic field at 3.5 K do not peak near the maximal density of magnetic bubbles. The results unambiguously evidence that the UAHE in $\text{Mn}_x\text{Ga}/\text{Pt}$ bilayers shows no correlation with chiral spin structures but is driven by the modified interfacial properties due to the emergence of strong interfacial SOC introduced by Pt. The origins of the UAHE have been explored including the modified Berry curvatures, the skew scattering, and the possible Weyl fermion states.

II. METHODS

For this study, we prepared magnetic bilayers of Mn_xGa 6 nm/Pt 5 nm 5 nm ($x = 1.0, 1.25, 1.55$) and a reference sample of Mn_xGa 6 nm/Al 5 nm (see also Methods). The nominal 1-nm-thick Mn_xGa films were first grown on 100-nm-thick GaAs buffered semi-insulating GaAs (001) substrates by molecular-beam epitaxy with controlling the flux of Mn and Ga atoms. The growth temperature was set at 70 °C. Then the films were annealed at 300 °C for 1 min, and other nominal 5-nm-thick Mn_xGa films continued to be grown at 300 °C after the annealing. Finally, the films were transferred to the magnetron sputtering system immediately through a lower vacuum chamber, and 5-nm-thick Al and Pt films were deposited on the Mn_xGa films. All the films have been patterned into Hall bars in the size of $10\ \mu\text{m} \times 80\ \mu\text{m}$ using photolithography and Ar ion milling. Similar to our previous work [15–17], both the Hall resistivity and longitudinal resistivity in this work were determined by extracting the contributions of the Mn_xGa single layer by assuming a parallel resistor model.

III. RESULTS AND DISCUSSION

By subtracting the H -linear ordinary Hall term ($\rho_0 = R_0H$) from the total Hall resistivity ρ_{XY} , we have obtained the sum of other Hall contributions of the $\text{Mn}_x\text{Ga}/\text{Pt}$ bilayers under perpendicularly applied magnetic field H as shown in Figs. 1(a)–1(c). Bumps or dips emerge in the whole temperature range from 5 to 300 K for all three bilayers. Figures 1(d)–1(f) show the temperature dependence of magnetoresistance (MR), $MR = [\rho_{XX}(H) - \rho_{XX}(0)]/\rho_{XX}(0)$, under perpendicular magnetic field. The sign of MR changes from negative to positive as the temperature decreases. Both the Hall and longitudinal signals are quite different from those of $\text{Mn}_x\text{Ga}/\text{Al}$ bilayers (see Supplemental Material, Fig. S1 [18]), in which the transport properties are determined by the single Mn_xGa layers [17]. Compared to $\text{Mn}_x\text{Ga}/\text{Al}$, the $\text{Mn}_x\text{Ga}/\text{Pt}$ bilayers show distinct temperature dependences of anomalous Hall resistivity ρ_A and longitudinal resistivity ρ_{XX} (see Supplemental Material, Fig. S2 [18]). It is found that ρ_A can be described by scaling law $\rho_A = \alpha\rho_{XX} + b\rho_{XX}^2$ with ρ_{XX} for the $\text{Mn}_x\text{Ga}/\text{Al}$ bilayers (see Supplemental Material, Fig. S2 [18]), where α and b denote extrinsic skew scattering and intrinsic mechanism respectively, ρ_{XX0} is the residual resistivity induced by impurity scattering [19,20]. Here, we have used the longitudinal resistivity measured at 5 K as the residual resistivity ρ_{XX0} . We believe that 6-nm Mn_xGa is thick enough to prevent the deterioration of its bulk magnetic properties, and new magnetic states or transport features are

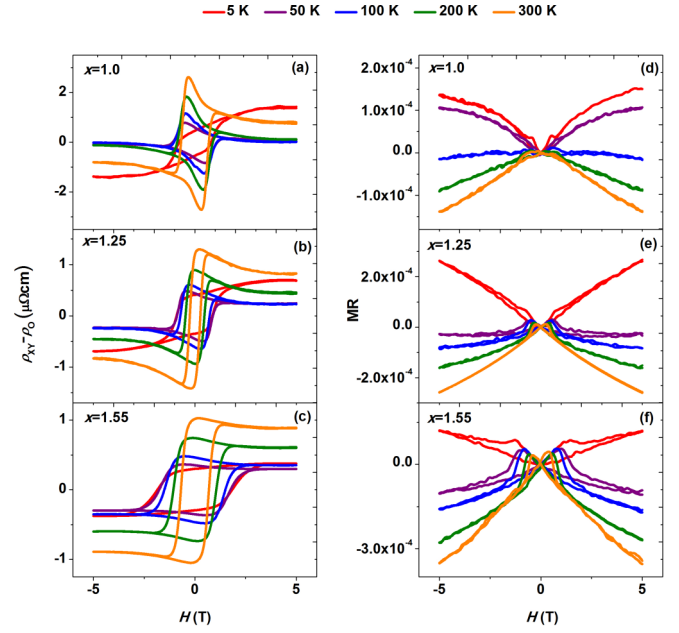


FIG. 1. (a–c) The Hall resistivities after subtracting ordinary Hall contributions ($\rho_{XY} - \rho_0$) of the $\text{Mn}_x\text{Ga}/\text{Pt}$ bilayers under perpendicularly applied magnetic fields in the temperature range from 5 to 300 K; (d–f) MR of the $\text{Mn}_x\text{Ga}/\text{Pt}$ bilayers under perpendicularly applied magnetic fields in the temperature range from 5 to 300 K.

expected to be of interfacial nature. Then, we attempt to investigate the anomalous Hall effect (AHE) in the $\text{Mn}_x\text{Ga}/\text{Pt}$ bilayers using the same scaling law. Figures 2(a)–2(c) show the experimental and fitted relationships between ρ_A and ρ_{XX}^2 . At relatively high temperatures, the scaling law is found to work only for large ρ_{XX} . The slope b of the $\text{Mn}_x\text{Ga}/\text{Pt}$ bilayers is similar to that in the $\text{Mn}_x\text{Ga}/\text{Al}$ bilayers with the same Mn component x , indicating the same intrinsic nature of the Mn_xGa films. In the low-temperature limit, there are large

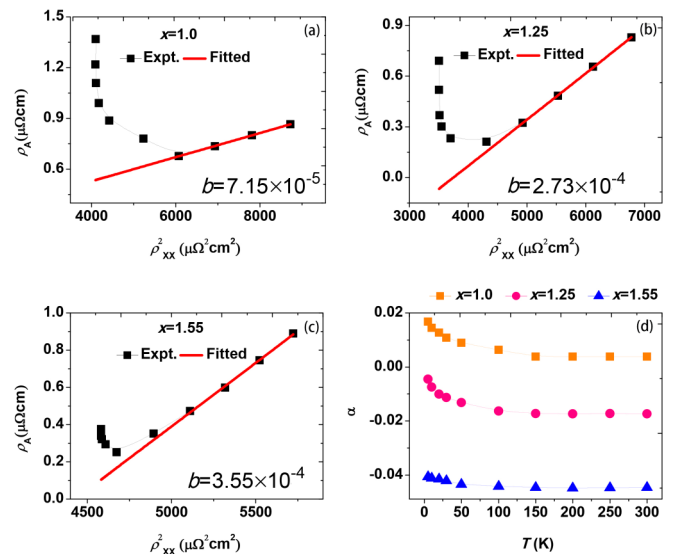


FIG. 2. (a–c) ρ_A vs ρ_{XX}^2 for $\text{Mn}_x\text{Ga}/\text{Pt}$ bilayers. Solid red lines refer to a linear fit of $\rho_A = \alpha\rho_{XX} + b\rho_{XX}^2$. (d) Temperature dependence of skew scattering coefficients α for $\text{Mn}_x\text{Ga}/\text{Pt}$ bilayers.

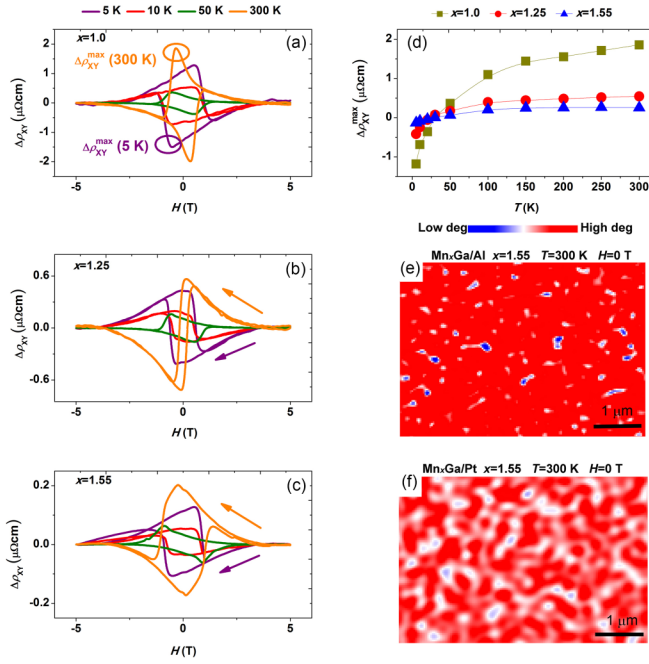


FIG. 3. (a–c) The additional Hall resistivities after subtracting ordinary and anomalous Hall contributions $\Delta\rho_{XY}$ of the $\text{Mn}_x\text{Ga}/\text{Pt}$ bilayers as functions of perpendicularly applied magnetic fields at different temperatures from 5 to 300 K. $\Delta\rho_{XY}^{\max}$ denotes the peak (300 K) or valley (5 K) values with sweeping magnetic field from positive to negative. (d) Temperature dependence of $\Delta\rho_{XY}^{\max}$ for the $\text{Mn}_x\text{Ga}/\text{Pt}$ bilayers. Lines are provided to guide the eye. Magnetic force microscopy images for the $\text{Mn}_{1.55}\text{Ga}/\text{Al}$ (e) and $\text{Mn}_{1.55}\text{Ga}/\text{Pt}$ bilayers (f) at 300 K after applying a positive perpendicular magnetic field of 5 T and then decreasing the magnetic field down to zero. The scale size is $7\mu\text{m} \times 5\mu\text{m}$.

positive deviations, which should be ascribed to the increase of ρ_A since ρ_{XX} decreases monotonically with decreasing temperature and then approaches a constant due to weak Kondo effect (see Supplemental Material, Fig. S3 [18]). The upturn of ρ_A is indicative of the onset of large extrinsic skew scattering due to the strong SOC of impurities. The values of α in the low-temperature limit can be determined from the experimental data based on the equation $\rho_A = \alpha\rho_{XX0} + b\rho_{XX}^2$, in which the values of b are the slopes of the fitted lines as shown in Figs. 2(a) and 2(b). At finite temperature, the values of α are determined from the intercept of the fitted lines. The temperature dependence of α has been shown in Fig. 2(d), and a deviation has been found in the low-temperature limit.

After subtracting ordinary and anomalous Hall signals, we can get additional Hall resistivities $\Delta\rho_{XY} = \rho_{XY} - \rho_0 - \rho_A$ as shown in Figs. 3(a)–3(c), and the shapes of $\Delta\rho_{XY}(H)$ reverse in the low-temperature limit with sweeping magnetic field from positive to negative. The temperature dependences of the largest $\Delta\rho_{XY}$ ($\Delta\rho_{XY}^{\max}$) in all the bilayers have been shown in Fig. 3(d), and a sign change is observed for all the bilayers at low temperature. Here, we use MFM to determine the correspondence of transport features with the spin structures. Figure 3(e) shows an illustrative example of such images in the $\text{Mn}_{1.55}\text{Ga}/\text{Al}$ bilayers after saturating with a positive magnetic field of $H = 5$ to 0 T at 300 K.

The magnetization is almost fully aligned in the positive magnetic field direction and the MFM image shows several magnetic bubbles. For the $\text{Mn}_{1.55}\text{Ga}/\text{Pt}$ bilayers as shown in Fig. 3(f), a dilute density of small magnetic bubbles in the size of 100–200 nm has emerged among the wormlike or the long-stripes patterns. This suggests that the magnetic bubbles have emerged in both the $\text{Mn}_{1.55}\text{Ga}/\text{Al}$ and $\text{Mn}_{1.55}\text{Ga}/\text{Pt}$ bilayers, while only the latter exhibits nonzero $\Delta\rho_{XY}$ at the zero magnetic field. The most different mechanisms in these two bilayers is that a strong interfacial SOC is only introduced in $\text{Mn}_{1.55}\text{Ga}/\text{Pt}$ bilayers, which will profoundly modify both the magnetic and transport features. The magnetic bubble is a kind of magnetic domain phase in FM, which can be established through the competition between long-range dipolar and short-range exchange interactions. It is not a large skyrmion since it can be either topologically protected (chiral) or not (achiral). In the presence of interfacial DMI induced by strong SOC, the domain wall configuration in the $\text{Mn}_{1.55}\text{Ga}/\text{Pt}$ bilayers may be of Néel type with fixed chirality [21]. On the contrary, in the $\text{Mn}_{1.55}\text{Ga}/\text{Al}$ bilayers that lack interfacial DMI, the magnetic bubbles were solely stabilized by strong dipole interactions that give rise to a rich collection of spin structures with nonuniform spin chirality [22]. Therefore, the chirality of the spin structures in the $\text{Mn}_x\text{Ga}/\text{Pt}$ bilayers cannot be identified, and we first speculate that the nonzero $\Delta\rho_{XY}(0)$ at 300 K in $\text{Mn}_{1.55}\text{Ga}/\text{Pt}$ bilayers is the THE.

Before the discussion of the possible THE, we should elucidate whether the nonzero $\Delta\rho_{XY}$ in the $\text{Mn}_x\text{Ga}/\text{Pt}$ bilayers was described in the strong (adiabatic approximation) or weak coupling (nonadiabatic approximation) regime. In this work, we use the model developed by Nakazawa *et al.* [12,23], which considers three regimes depending on the strength of the exchange coupling. The three regimes correspond to different conditions between several important system parameters, such as the characteristic length scale of the chiral spin structures q^{-1} , the electron mean free path l , the momentum relaxation time $\tau = \frac{m^*}{e^2\rho_{XX}n} = \frac{m^*R_0}{e\rho_{XX}}$, and the exchange time $\tau_{ex} = \frac{\hbar}{2J}$. Here, m^* is the effective electron mass, R_0 is the ordinary Hall coefficient (see Supplemental Material, Fig. S4 [18]), and J is the exchange coupling constant. The spin-resolved band structures of $L1_0\text{-MnGa}$ without SOC have been calculated using first-principles calculations (see Supplemental Material, Fig. S5 [18]), and we get $E_F = 5.2712$ eV, $m^* = 0.65m_0$, $J = 1.1$ eV, and $k_F = 0.121$ nm $^{-1}$. Then, we get the corresponding constant of the $\text{Mn}_{1.55}\text{Ga}/\text{Pt}$ bilayers at 300 K, $l = \frac{6\pi^2\hbar}{e^2\rho_{XX}k_F^2} = 1.1$ nm, $\tau = 6 \times 10^{-11}$ s, and $\tau_{ex} = 3.8 \times 10^{-16}$ s. It is found that the adiabatic approximation is applicable since $\tau_{ex} \ll \tau$ and $(ql)^2 < 1$, indicating the spin of the conduction electrons can adiabatically follow the surrounding local magnetization. Therefore, the additional Hall signals can be written as $\Delta\rho_{XY} = PR_0B_{\text{eff}} = PR_0n_{\phi}^T\phi_0$, where P is the spin polarization of charge carriers and determined to be 20% according to the band structures, B_{eff} the fictitious magnetic field, $\phi_0 = h/e$ the flux quantum, and n_{ϕ}^T the density of chiral spin structures [2]. Then the n_{ϕ}^T of the $\text{Mn}_{1.55}\text{Ga}/\text{Pt}$ bilayers at 300 K is calculated to be $75\mu\text{m}^{-2}$ and the separation of the chiral spin structures $[(n_{\phi}^T)^{-1/2}]$ is ~ 115 nm. Obviously, it reveals a large discrepancy as compared with

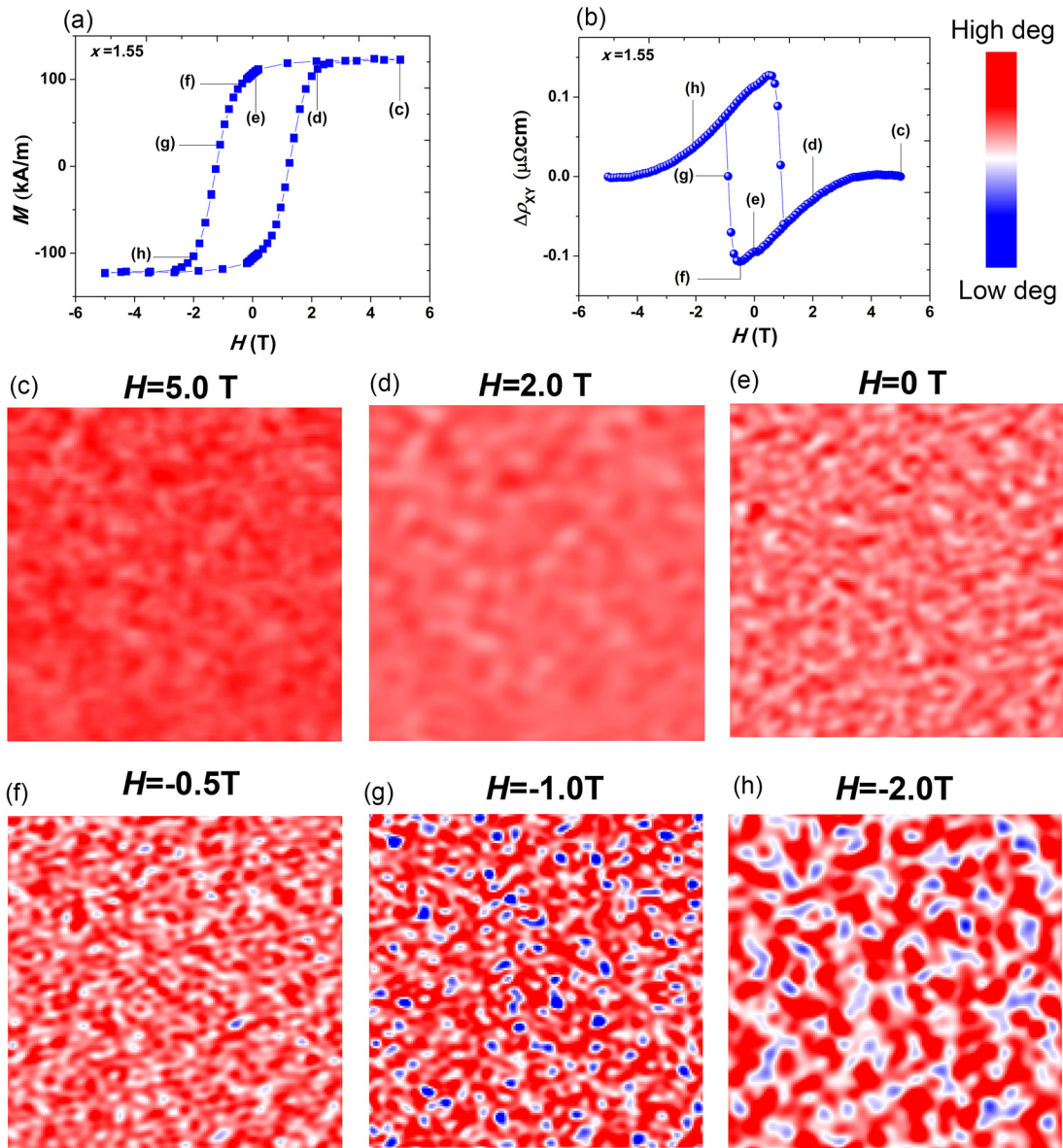


FIG. 4. M - H (a) and $\Delta\rho_{XY}$ - H (b) curves for $\text{Mn}_{1.55}\text{Ga}/\text{Pt}$ bilayers at 3.5 K. (c-h) Magnetic force microscopy images after applying a positive perpendicular magnetic field of 5 T and then decreasing the magnetic field down to +2 T, 0 T, -0.5 T, -1.0 T, and -2.0 T, respectively. The scale size is $7\ \mu\text{m} \times 7\ \mu\text{m}$.

the MFM results, indicating the AHE in $\text{Mn}_x\text{Ga}/\text{Pt}$ bilayers should be much more involved.

A large discrepancy between MFM and transport features has also been found at low temperatures. The magnetic field-dependent MFM, M - H and $\Delta\rho_{XY}$ - H curves of the $\text{Mn}_{1.55}\text{Ga}/\text{Pt}$ bilayers at 3.5 K have been compared as shown in Fig. 4 to gain more insight into the nature of the spin structures and transport features. The magnetization is almost fully aligned in the positive magnetic field direction with $H = 5$ T and $\Delta\rho_{XY}$ is suppressed as shown in Figs. 4(a) and 4(b), respectively, and the MFM image shows a homogeneous red contrast as shown in Fig. 4(c). The $\Delta\rho_{XY}$ first decreased from zero to negative values with sweeping the magnetic field from the positive. Although the MFM image is almost the same comparing between 5 and 2 T, the value of $\Delta\rho_{XY}$ is obviously nonzero at 2 T. At the remanent state, the

MFM image shows obscure wormlike configurations in the so-called labyrinthine state. As H decreases further towards large negative values, -0.5 T, the wormlike or the long-stripes patterns become clear, among which several bubblelike magnetic domains have emerged. With further decreasing the magnetic field to -1.0 T, which is around the coercivity, many isolated bubblelike magnetic domains of a typical size of ~ 50 - 200 nm have been observed, while the value of $\Delta\rho_{XY}$ has approached to be zero. By the way, the same MFM measurements have also been carried out in the $\text{Mn}_{1.55}\text{Ga}/\text{Al}$ bilayers at 3.5 K (see Supplemental Material, Fig. S6 [18]). A similar magnetic field-dependent MFM result has also been found in the $\text{Mn}_{1.55}\text{Ga}/\text{Al}$ bilayers, while there are no bump/dip features of Hall signals (see Supplemental Material, Fig. S1 [18]). It reveals that the magnetic bubbles, in the form of up-magnetized domains in a down-magnetized background

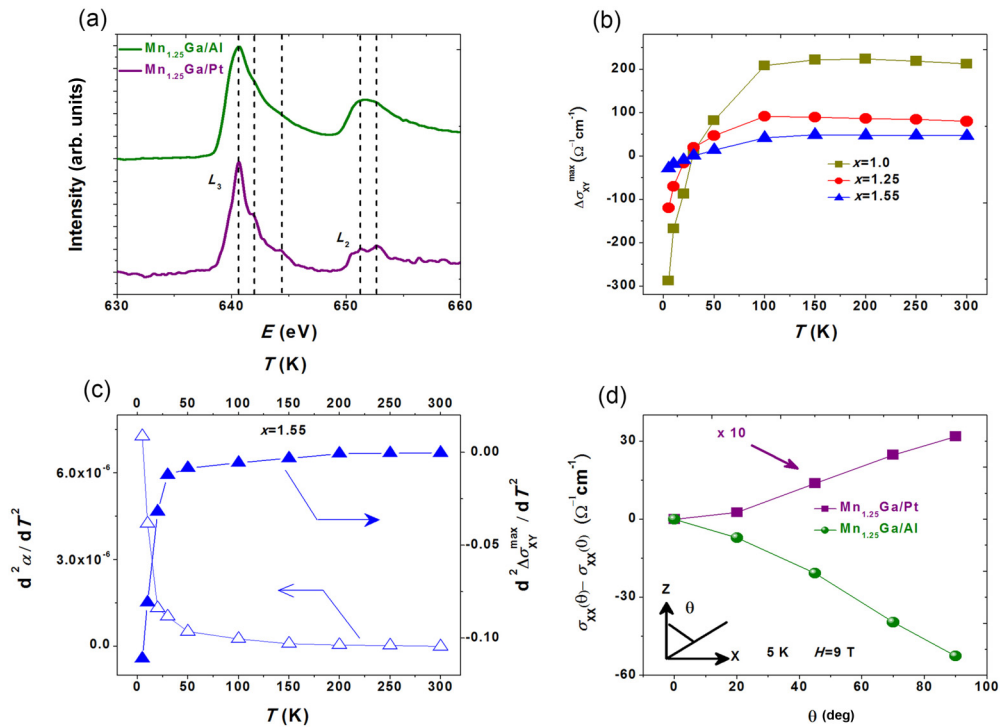


FIG. 5. (a) Mn $2p$ XAS spectra of the $\text{Mn}_{1.25}\text{Ga}/\text{Pt}$ and $\text{Mn}_{1.25}\text{Ga}/\text{Al}$ bilayers. (b) Temperature dependence of $\Delta\sigma_{XY}^{\max}$ for the $\text{Mn}_x\text{Ga}/\text{Pt}$ bilayers. (c) Temperature dependence of $d^2\Delta\sigma_{XY}^{\max}/dT^2$ and $d^2\alpha/dT^2$ for the $\text{Mn}_{1.55}\text{Ga}/\text{Pt}$ bilayers. (d) Angle dependence of $[\sigma_{XX}(\theta) - \sigma_{XX}(0)]$ at 5 K for $\text{Mn}_{1.25}\text{Ga}/\text{Al}$ and $\text{Mn}_{1.25}\text{Ga}/\text{Pt}$ bilayers. The current is applied along the X direction, and $\theta = 0^\circ$ denotes the magnetic field (9 T) is applied along the Z direction. The signals in $\text{Mn}_{1.25}\text{Ga}/\text{Pt}$ bilayers are multiplied by a factor of 10 shown as “ $\times 10$.”

of a perpendicular magnetic anisotropy Mn_xGa films, are considered to be stabilized by magnetic dipole interactions, which should be achiral. Therefore, the THE which is the hallmark of chiral spin structures is unlikely to be the origin of the bump/dip features of Hall signals in the $\text{Mn}_x\text{Ga}/\text{Pt}$ bilayers.

In the following discussion, the additional Hall signals in the $\text{Mn}_x\text{Ga}/\text{Pt}$ bilayers have been termed as UAHE, which should be strongly related to the strong interfacial SOC as compared with $\text{Mn}_x\text{Ga}/\text{Al}$ bilayers. To further investigate the modified interfacial properties, the Mn $2p$ -x-ray absorption spectroscopy (XAS) spectra were recorded at room temperatures in the total electron yield (TEY) mode by measuring the drain current of the electrically isolated sample as shown in Fig. 5(a). The XAS spectra of Mn atoms should mainly come from the interfaces, since it is well known that the TEY detection is characterized by a probing depth lower than 5 nm (the Al and Pt layers are all 5 nm thick), and the number of electrons that reach the surface decays exponentially as a function of the depth of the photon absorption. In the spectra of the two bilayers, a sharp peak structure and a doublet structure are observed in the Mn $2p_{3/2}$ (L_3) and $2p_{1/2}$ (L_2) core excitation regions, respectively. In addition, some more evident shoulder structures are found on the larger-energy side of the $2p_{3/2}$ component in the $\text{Mn}_{1.25}\text{Ga}/\text{Pt}$ bilayers, which is a characteristic of primarily d^5 with some d^6 ground states [24,25]. The distinctly split structure of the $2p_{1/2}$ component has also been found, and it is similar to antiferromagnetic MnPt films and submonolayer deposition of Mn on Cu, where the Mn $3d$ orbitals are more localized than in the bulk [26]. On the other hand, by comparison, the featureless spectrum of the Mn in

MnGa/Al bilayers makes us confident that the double-peak structure of L_2 in MnGa/Pt bilayers is not caused by contamination. It indicates a significant influence of the coordination on the electronic structure of Mn d states at the interface of the $\text{Mn}_x\text{Ga}/\text{Pt}$ bilayers. Though the Pt has high spin susceptibility originating from the large Stoner exchange parameter, a very small magnetic moment in Pt is considered to be induced at the interfaces [27]. However, the magnetic ground state of Mn is antiferromagnetic, and a large negative nearest-neighbor exchange interaction has been theoretically confirmed by Belabbes *et al.* [27]. Therefore, the interfacial ferromagnetic states of Mn_xGa will be tremendously modified by the $3d$ - $5d$ orbital hybridization, leading to a combination of ferromagnetism and the antiferromagnetism at the interface. Consequently, the evolution of the electronic structure due to modulated magnetic states at the interfaces will generate significant momentum-space Berry phase contributions to the AHE at finite temperature. At high magnetic field, the interfacial antiferromagnetism was annihilated and only the ferromagnetism that dominates the AHE will be induced. At around zero magnetic field, although the emergent antiferromagnetism has vanishingly small magnetization and has not varied the remanent magnetization of Mn_xGa (see Supplemental Material, Fig. S4 [18]), the modified momentum-space Berry curvature at the interface will contribute a large anomalous Hall signal, analogous to the recently reported large AHE in the antiferromagnets Mn_3Sn , GdPtBi , and Mn_3Ge [28–30]. The phenomenon may also depend on the surface roughness of Mn_xGa , since the largest UAHE has been found for $x = 1.0$, which also shows the largest surface roughness (see

Supplemental Material, Fig. S7 [18]). The increased surface roughness may decrease the directional arrangement of magnetic moment of Mn_xGa and assist the emergence of antiferromagnetism. Furthermore, the formation of long-range skyrmion lattices at the interfaces can be prevented by large surface roughness, since it may enhance the magnetic dipole energy which will dominate the interfacial DMI and favors achiral Bloch walls [31,32], although it has been theoretically proved that the spin-flip excitations through SOC in half-filled or high-spin $3d$ overlayer (Mn) make the largest contribution to DMI [27]. For further physical insight, we show the temperature dependence of the largest additional Hall conductivity $\Delta\sigma_{XY}^{\max}$ which is defined as $\Delta\rho_{XY}^{\max}/\rho_{XX}^2$, as shown in Fig. 5(b). Phenomenological reasoning suggests that the longitudinal conductance increases with decreasing temperature while $\Delta\sigma_{XY}^{\max}$ remains almost constant at the high-temperature regime which should stem from the intrinsic contributions (momentum-space Berry curvatures). In the low-temperature limit, $\Delta\sigma_{XY}^{\max}$ reveals a sharp decrease to large negative values. We have plotted the temperature dependence of $d^2\Delta\sigma_{XY}^{\max}/dT^2$ and $d^2\alpha/dT^2$ as shown in Fig. 5(c), which shows sharp variations at almost the same temperature (50 K). Notably, the aforementioned skew scattering contribution dominates the AHE in the low-temperature limit as shown in Fig. 2. Therefore, the sign change of UAHE should be related to the skew scattering due to the emergence of strong interfacial SOC, which depends on the distribution, the type, and the density of impurities [33–35]. Since the sign of the skew scattering contribution changes when that of the scattering potential is reversed, the impurity potential is considered to be modified through the emergence of antiferromagnetic states at around zero magnetic fields. Further theoretical work is necessary to accurately describe this complex correlation of UAHE and $3d$ - $5d$ orbital hybridization in the FM/HM bilayers.

In addition, we want to mention another possible role of the strong interfacial SOC introduced by Pt. It is known that, in materials with heavy elements, the band inversion can be induced since the strong SOC can split the p band by a large enough magnitude to flip the s - p band structure, leading to a topological insulator [36]. The inverted bulk band structure will topologically give rise to metallic surface states, which have a nearly linear energy-momentum relationship. Interestingly, the topological surface states also exist on the surface of Weyl metals, in which the bulk bands are gapped by SOC in the momentum space except at Weyl or Dirac nodes. In the case of the $\text{Mn}_x\text{Ga}/\text{Pt}$ bilayers, we also suppose the emergence of Weyl metallic features at the interfaces, which may explain the positive MR in the low-temperature limit as shown in Fig. 1. The chiral anomaly is predicted to occur in Weyl metals since the conservation of chiral charges is violated in the case of a parallel magnetic and electric field, resulting in a negative longitudinal MR [37,38]. This suggests that there is a current along the magnetic field arising from the unequal occupation of left and right moving chiral modes, giving a

current of $j_c \propto \mathbf{BE} \cdot \mathbf{B}$, where \mathbf{E} and \mathbf{B} are the external electric and magnetic field, respectively [34,35]. Then the electric currents measured in a thin film with chiral anomaly inevitably include this additional contribution. In the case of \mathbf{E}/\mathbf{B} , the total electric current should be the largest and the resistance is the smallest. Figure 5(d) shows the angular dependence of the $[\sigma_{XX}(\theta) - \sigma_{XX}(0)]$ in the $\text{Mn}_{1.25}\text{Ga}/\text{Pt}$ and $\text{Mn}_{1.25}\text{Ga}/\text{Pt}$ bilayers. The applied current is along the X axis, and the magnetic field of 9 T is applied in the ZX plane with angle θ relative to the Z axis. We have observed the decrease of $[\sigma_{XX}(\theta) - \sigma_{XX}(0)]$ in the $\text{Mn}_{1.25}\text{Ga}/\text{Al}$ bilayers as increasing θ , reflecting the anisotropic magnetoresistance of the single $\text{Mn}_{1.25}\text{Ga}$ layer as shown in our previous work [39]. However, the values in the $\text{Mn}_{1.25}\text{Ga}/\text{Pt}$ bilayers have been enhanced with increasing θ , which is consistent with the assumption that there is an additional electric current in the $\text{Mn}_{1.25}\text{Ga}/\text{Pt}$ bilayers and it is the largest when \mathbf{E}/\mathbf{B} . Therefore, these transport features may be related to the Weyl fermions at the $\text{Mn}_x\text{Ga}/\text{Pt}$ interfaces. Recent theory and experiments have suggested that the Weyl fermions with broken time-reversal symmetry were also expected to generate strong intrinsic AHE [40,41], which may also contribute to the UAHE in the low-temperature limit. However, the transport properties of our bilayer systems are more complicated since bulk Pt, bulk Mn_xGa , and $\text{Mn}_x\text{Ga}/\text{Pt}$ interfaces will all contribute to the transport features (see Supplemental Material, Fig. S8 [18]). Other mechanisms including orbital magnetoresistance are hard to distinguish [42]. It is beyond the discussion of this work and would be interesting to verify the possibility of interface-driven Weyl fermion states in future studies.

IV. CONCLUSION

In conclusion, we have discussed the origin of interface-driven UAHE in the $\text{Mn}_x\text{Ga}/\text{Pt}$ bilayers, which was distinguished from the THE related to chiral spin structures through comparing the magnetic field-dependent MFM and transport features at low temperatures. We firmly demonstrate that the bump/dip features of Hall signals in FM/HM heterostructures cannot be taken as an unambiguous signature for chiral spin structures, and it should be treated discreetly since a wealth of underlying and interesting physics is often regrettably missed. It further demonstrates that an extraordinary range of unanticipated phenomena is expected to emerge from the interfaces, exciting new scientific results and functionality for future research.

ACKNOWLEDGMENTS

This work was partially supported by the National Science Foundation of China (Grants No. 51971027, No. 51731003, No. 51671019, No. 51602022, No. 61674013, No. 51602025, and No. 11675023), and the Fundamental Research Funds for the Central Universities (Grants No. FRF-TP-19-001A3, No. FRF-BD-18-014A, and No. FRF-GF-17-B6).

[1] F. Hellman, A. Hoffmann, Y. Tserkovnyak, G. S. D. Beach, E. E. Fullerton, C. Leighton, A. H. MacDonald, D. C. Ralph, D. A. Arena, H. A. Dürr, P. Fischer, J. Grollier, J. P. Heremans,

T. Jungwirth, A. V. Kimel, B. Koopmans, I. N. Krivorotov, S. J. May, A. K. Petford-Long, J. M. Rondinelli *et al.*, *Rev. Mod. Phys.* **89**, 025006 (2017).

- [2] A. Soumyanarayanan, N. Reyren, A. Fert, and C. Panagopoulos, *Nature* **539**, 509 (2016).
- [3] A. Fert, N. Reyren, and V. Cros, *Nat. Rev. Mater.* **2**, 17031 (2017).
- [4] Y. Tokura, M. Kawasaki, and N. Nagaosa, *Nat. Phys.* **13**, 1056 (2017).
- [5] I. Dzyaloshinsky, *J. Phys. Chem. Solids* **4**, 241 (1958).
- [6] T. Moriya, *Phys. Rev.* **120**, 91 (1960).
- [7] N. Nagaosa and Y. Tokura, *Nat. Nanotechnol.* **8**, 899 (2013).
- [8] P. Bruno, V. K. Dugaev, and M. Taillefumier, *Phys. Rev. Lett.* **93**, 096806 (2004).
- [9] N. Nagaosa, J. Sinova, S. Onoda, A. H. MacDonald, and N. P. Ong, *Rev. Mod. Phys.* **82**, 1539 (2010).
- [10] Y. Taguchi, Y. Oohara, H. Yoshizawa, N. Nagaosa, and Y. Tokura, *Science* **291**, 2573 (2001).
- [11] G. Tatara and H. Kawamura, *J. Phys. Soc. Jpn.* **71**, 2613 (2002).
- [12] K. Nakazawa and H. Kohno, *J. Phys. Soc. Jpn.* **83**, 073707 (2014).
- [13] M. Onoda, G. Tatara, and N. Nagaosa, *J. Phys. Soc. Jpn.* **73**, 2624 (2004).
- [14] K. S. Denisov, I. V. Rozhansky, N. S. Averkiev, and E. Lähderanta, *Phys. Rev. Lett.* **117**, 027202 (2016).
- [15] K. K. Meng, X. P. Zhao, P. F. Liu, Q. Liu, Y. Wu, Z. P. Li, J. K. Chen, J. Miao, X. G. Xu, J. H. Zhao, and Y. Jiang, *Phys. Rev. B* **97**, 060407(R) (2018).
- [16] K. K. Meng, J. Miao, X. G. Xu, J. X. Xiao, J. H. Zhao, and Y. Jiang, *Phys. Rev. B* **93**, 060406(R) (2016).
- [17] K. K. Meng, J. Miao, X. G. Xu, Y. Wu, X. P. Zhao, J. H. Zhao, and Y. Jiang, *Phys. Rev. B* **94**, 214413 (2016).
- [18] See Supplemental Material at <http://link.aps.org/supplemental/10.1103/PhysRevB.100.184410> for more detailed discussion of the magnetic and transport properties.
- [19] Y. Tian, L. Ye, and X. Jin, *Phys. Rev. Lett.* **103**, 087206 (2009).
- [20] L. J. Zhu, D. Pan, and J. H. Zhao, *Phys. Rev. B* **89**, 220406(R) (2014).
- [21] A. Thiaville, S. Rohart, E. Jué, V. Cros, and A. Fert, *Europhys. Lett.* **100**, 57002 (2012).
- [22] W. Jiang, G. Chen, K. Liu, J. Zang, S. G. E. te Velthuis, and A. Hoffmann, *Phys. Rep.* **704**, 1 (2017).
- [23] K. Nakazawa, M. Bibes, and H. Kohno, *J. Phys. Soc. Jpn.* **87**, 033705 (2018).
- [24] A. Kimura, S. Suga, T. Shishidou, S. Imada, T. Muro, S. Y. Park, T. Miyahara, T. Kaneko, and T. Kanomata, *Phys. Rev. B* **56**, 6021 (1997).
- [25] A. Chakrabarti, C. Biswas, S. Banik, R. S. Dhaka, A. K. Shukla, and S. R. Barman, *Phys. Rev. B* **72**, 073103 (2005).
- [26] J. Fujii, F. Borgatti, G. Panaccione, M. Hochstrasser, F. Maccherozzi, G. Rossi, and G. van der Laan, *Phys. Rev. B* **73**, 214444 (2006).
- [27] A. Belabbes, G. Bihlmayer, F. Bechstedt, S. Blügel, and A. Manchon, *Phys. Rev. Lett.* **117**, 247202 (2016).
- [28] S. Nakatsuji, N. Kiyohara, and T. Higo, *Nature* **527**, 212 (2015).
- [29] T. Suzuki, R. Chisnell, A. Devarakonda, Y.-T. Liu, W. Feng, D. Xiao, J. W. Lynn, and J. G. Checkelsky, *Nat. Phys.* **12**, 1119 (2016).
- [30] A. K. Nayak, J. E. Fischer, Y. Sun, B. Yan, J. Karel, A. C. Komarek, C. Shekhar, N. Kumar, W. Schnelle, and J. Kübler *et al.*, *Sci. Adv.* **2**, e1501870 (2016).
- [31] Z. Hou, W. Ren, B. Ding, G. Xu, Y. Wang, B. Yang, Q. Zhang, Y. Zhang, E. Liu, F. Xu, W. Wang, G. Wu, X. Zhang, B. Shen, and Z. Zhang, *Adv. Mater.* **29**, 1701144 (2017).
- [32] Y.-P. Zhao, G. Palasantzas, G.-C. Wang, and J. Th. M. De Hosson, *Phys. Rev. B* **60**, 1216 (1999).
- [33] W. L. Lee, S. Watauchi, V. L. Miller, R. J. Cava, and N. P. Ong, *Science* **303**, 1647 (2004).
- [34] W. J. Fan, L. Ma, and S. M. Zhou, *J. Phys. D: Appl. Phys.* **48**, 195004 (2015).
- [35] S. Zhang, *Phys. Rev. B* **51**, 3632 (1995).
- [36] B. Yan and C. Felser, *Annu. Rev. Condens. Matter Phys.* **8**, 337 (2017).
- [37] X. Huang, L. Zhao, Y. Long, P. Wang, D. Chen, Z. Yang, H. Liang, M. Xue, H. Weng, Z. Fang, X. Dai, and G. Chen, *Phys. Rev. X* **5**, 031023 (2015).
- [38] H. M. Weng, C. Fang, Z. Fang, B. A. Bernevig, and X. Dai, *Phys. Rev. X* **5**, 011029 (2015).
- [39] K. Meng, J. Xiao, Y. Wu, J. Miao, X. Xu, J. Zhao, and Y. Jiang, *Sci. Rep.* **6**, 20522 (2016).
- [40] M. Hirschberger, S. Kushwaha, Z. Wang, Q. Gibson, S. Liang, C. A. Belvin, B. A. Bernevig, R. J. Cava, and N. P. Ong, *Nat. Mater.* **15**, 1161 (2016).
- [41] E. Liu, Y. Sun, N. Kumar, L. Müchler, A. Sun, L. Jiao, S.-Y. Yang, D. Liu, A. Liang, Q. Xu, J. Kroder, V. Süß, H. Borrmann, C. Shekhar, Z. Wang, C. Xi, W. Wang, W. Schnelle, S. Wirth, Y. Chen *et al.*, *Nat. Phys.* **14**, 1125 (2018).
- [42] N. P. Armitage, E. J. Mele, and A. Vishwanath, *Rev. Mod. Phys.* **90**, 015001 (2018).